

Arctic Sea Ice Patterns Driven by the Asian Summer Monsoon

GARY GRUNSEICH

*Department of Atmospheric Sciences, and International Pacific Research Center,
University of Hawai'i at Mānoa, Honolulu, Hawaii*

BIN WANG

*Department of Atmospheric Sciences, and International Pacific Research Center, University of Hawai'i at Mānoa,
Honolulu, Hawaii, and Earth System Modeling Center, Nanjing University of Information Science and Technology,
Nanjing, China*

(Manuscript received 10 March 2016, in final form 6 September 2016)

ABSTRACT

The fluctuation of Arctic sea ice concentration (SIC) has been associated with changes in ocean circulation, ecology, and Northern Hemisphere climate. Prediction of sea ice melting patterns is of great societal interest, but such prediction remains difficult because the factors controlling year-to-year sea ice variability remain unresolved. Distinct monsoon–Arctic teleconnections modulate summer Arctic SIC largely by changing wind-forced sea ice transport. East Asian monsoon rainfall produces a northward-propagating meridional Rossby wave train extending into the Siberian Arctic. The Indian summer monsoon excites an eastward-propagating circumglobal teleconnection along the subtropical jet, reaching the North Atlantic before bifurcating into the Arctic. The remote Asian monsoon variations induce a dominant dipole sea ice melt pattern in which the North Atlantic–European Arctic contrasts with the Siberian–North American Arctic. The monsoon-related sea ice variations are complementary and comparable in magnitude to locally forced Arctic Oscillation variability. The monsoon–Arctic link will improve seasonal prediction of summer Arctic sea ice and possibly explain long-term sea ice trends associated with the projected increase in Asian monsoon rainfall over the next century.

1. Introduction

Changes in sea ice coverage have widespread influences on global ocean (Holland et al. 2001) and atmospheric circulation from seasonal to decadal time scales. Influences of spring Arctic sea ice on the East Asian summer monsoon (EASM; Guo et al. 2014), and the autumn sea ice in different regions of the Arctic on the strength of the winter Asian monsoon (Chen et al. 2014; Mori et al. 2014) have been identified. The decline of sea ice extent starting in

the late twentieth century has been linked to anomalous perturbations of the jet stream, which can alter midlatitude weather (Screen 2013; Francis and Vavrus 2012). The global impact of Arctic sea ice stresses the importance of determining the processes that control sea ice variability. Sea ice motion and concentration, on the other hand, are strongly driven by wind stress at distances far enough away from coastal effects (Thorndike and Colony 1982; Kimura and Wakatsuchi 2000). Sea ice primarily responds to the convergence of wind-driven ice transport and oceanic- and atmospheric-forced thermodynamic melt (Thorndike et al. 1975). Given that more than 70% of sea ice motion is explained by the geostrophic wind (Thorndike and Colony 1982), atmospheric circulation plays a fundamental role in shaping anomalous Arctic sea ice concentration patterns by modifying ice advection.

Beginning in the late twentieth century, the persistent decline in annual sea ice minimum extent has been well documented and the rapid sea ice reduction in the Arctic Ocean is widely attributed to anthropogenic climate change and dynamical and radiative feedbacks (IPCC

International Pacific Research Center Publication Number 1212,
School of Ocean and Earth Science and Technology Publication
Number 9826, and Earth System Modeling Center Publication
Number 127.

Corresponding author address: Bin Wang, Department of
Atmospheric Sciences, and International Pacific Research
Center, University of Hawai'i, 401 POST Bldg., 1680 East-West
Rd., Honolulu, HI 96822.
E-mail: wangbin@hawaii.edu

DOI: 10.1175/JCLI-D-16-0207.1

TABLE 1. List of years used for monsoon composites based on index phase.

EASM		ISM	
Positive	Negative	Positive	Negative
1988	1981	1980	1979
1992	1991	1983	1981
1994	1993	1988	1984
1997	1995	1992	1989
1999	1998	1994	1993
2007	2008	1997	1996
2009	2010	2003	1998
2011	2012	2011	2002
			2004
			2008
			2012

2013; Screen and Simmonds 2010; Hall 2004). Recently, the long-term trends in remote tropical variability and its impacts on anomalous Arctic atmospheric circulations are receiving extensive attention. The prominent warming over Canada and Greenland since 1979 is found to be strongly associated with a negative trend in the North Atlantic Oscillation, which is a response to an anomalous Rossby wave train originating in the tropical Pacific (Ding

et al. 2014). The interdecadal changes in the frequency of occurrence of individual Madden–Julian oscillations (Madden and Julian 1972) were found to have considerable influence on the Arctic warming (Yoo et al. 2011). Enhanced convection associated with the MJO in the tropical Indo-Pacific can produce poleward Rossby wave propagations that alter the heat and moisture transport as well as other atmospheric processes in the Arctic (Yoo et al. 2012). On synoptic time scales, a pathway has been identified in which atmospheric heating, the product of major Pakistan flooding events, has been directly linked to a rise in heat content in the Canadian Arctic roughly one week later due to advection throughout the troposphere (Krishnamurti et al. 2015). This pathway could link increasing rainfall across northwestern India in recent years and the rapid melting trend in Arctic ice. Tropical teleconnections invoke unique Arctic circulation changes over all seasons and on different time scales.

Reliable prediction of the anomalous sea ice patterns is of great global interest to numerous industries including maritime corporations, companies exploring energy and geological resources, fisheries, and local coastal communities concerned with adaptation and planning of resource

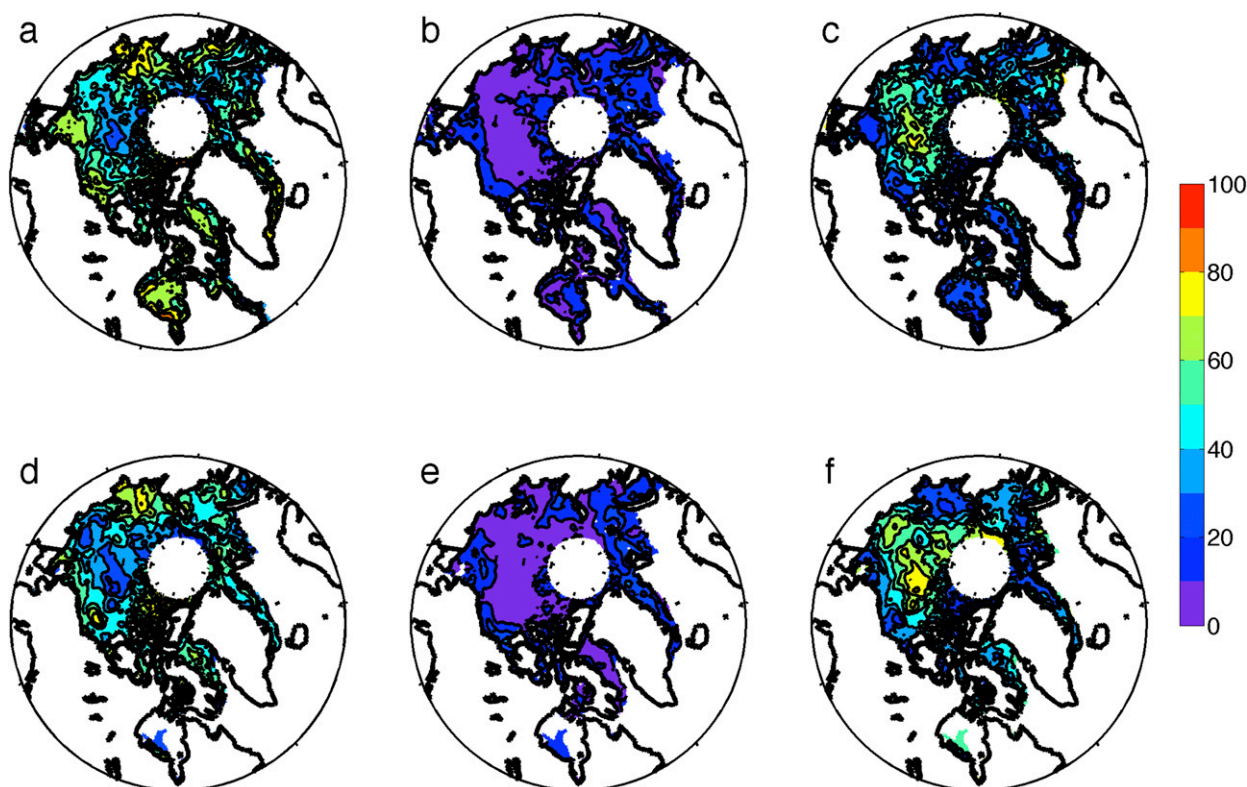


FIG. 1. Percent contributions to the overall (top) JJA and (bottom) ASO SIC variance using a Fourier harmonic transform for (a),(d) 2–5-yr periods; (b),(e) 5–8-yr periods; and (c),(f) >8-yr periods.

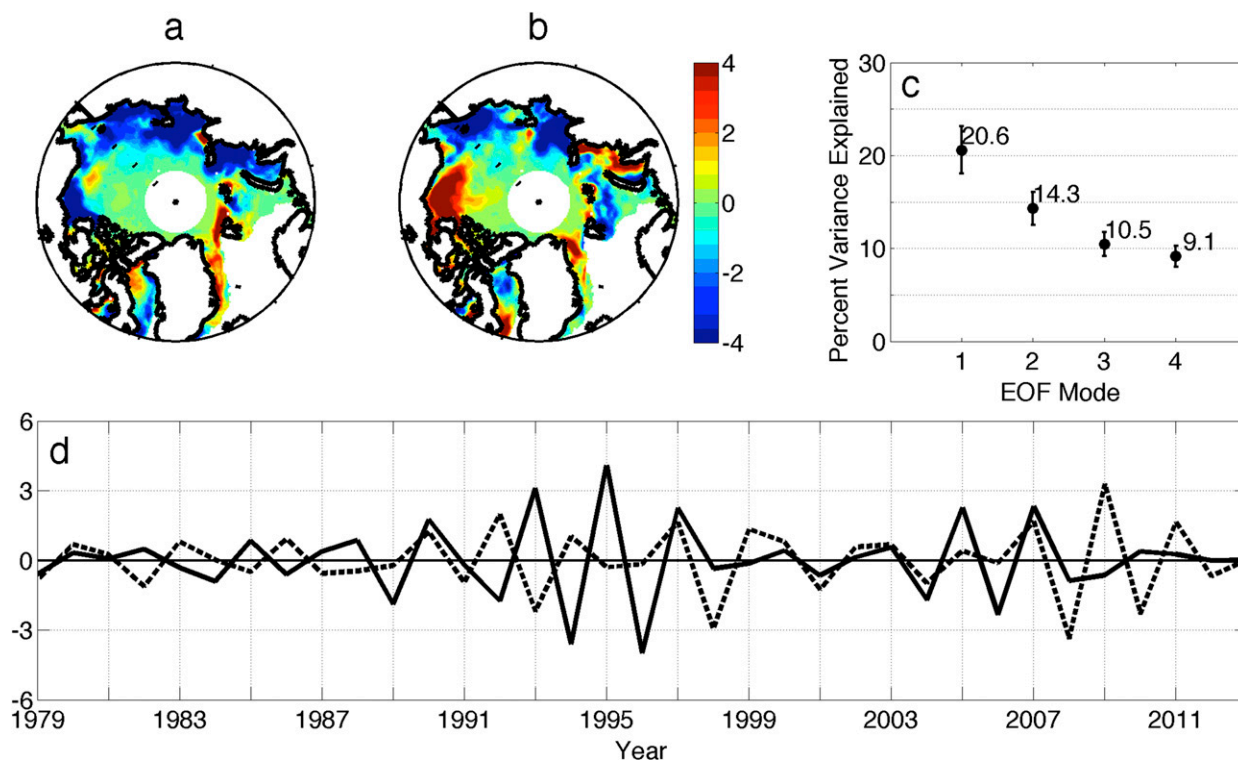


FIG. 2. (a) EOF1 and (b) EOF2 modes of JJA SIC with 3-yr running mean removed. Each pattern is standardized by the spatial standard deviation of each EOF. (c) The percentage of interannual variance explained by each EOF mode. Range bars show the sampling error for each EOF mode, which is a measure of separability. (d) Standardized time series of the EOF1 (solid) and EOF2 (dashed) modes.

usage. Yet, the year-to-year prediction has proven difficult (Kattsov et al. 2010; Stroeve et al. 2014). Natural interannual sea ice variability could be responsible for difficulties in prediction. Evidence is presented to show that summer Arctic sea ice concentration (SIC) variability is significantly modulated by the remote forcing from the EASM and Indian summer monsoon (ISM), identifying a new source of predictability for sea ice.

2. Data and methods

Climate Prediction Center (CPC) Merged Analysis of Precipitation (CMAP; Xie and Arkin 1997) data and the Global Precipitation Climatology Project (GPCP), version 2.2, combined precipitation dataset (Adler et al. 2003), both on a $2.5^\circ \times 2.5^\circ$ grid from 1979 to 2013, were averaged into one dataset similar to the methodology in Yim et al. (2014). The monsoon wave train patterns and resulting circulations utilize monthly ERA-Interim data winds, geopotential heights, and sea level pressure (SLP) to define the connection between each monsoon domain and the associated dynamics controlling sea ice patterns from 1979 to 2013. To determine the energy propagation along the teleconnection wave trains, regressed zonal departure anomalies are used to calculate

wave activity flux, which is parallel to the group velocity of the quasi-stationary Rossby waves (Plumb 1985).

To examine interannual sea ice variability during the boreal summer months, 1979–2013 bootstrap sea ice concentrations from the *Nimbus-7* Scanning Multichannel Microwave Radiometer (SMMR) and Defense Meteorological Satellite Program (DMSP) Special Sensor Microwave Imager–Special Sensor Microwave Imager/Sounder (SSM/I-SSMIS), version 2, were utilized (Comiso 2000). The bootstrap algorithm was chosen over the NASA Team algorithm due to the lower errors in the bootstrap algorithm data in melt/refreeze regions as well as thin ice areas, which would be much more prevalent during the summer.

Sea ice thickness and motion data came from the Pan-Arctic Ice–Ocean Modeling and Assimilation System (PIOMAS) for the 1979–2013 time period (Zhang and Rothrock 2003). Sea ice advection and sea ice growth rate were also utilized to understand the major terms governing sea ice thickness (Thorndike et al. 1975).

Monsoon indices and their relations with the SIC EOF2

To investigate the relationship between the EASM and ISM interannual variability and polar circulations,

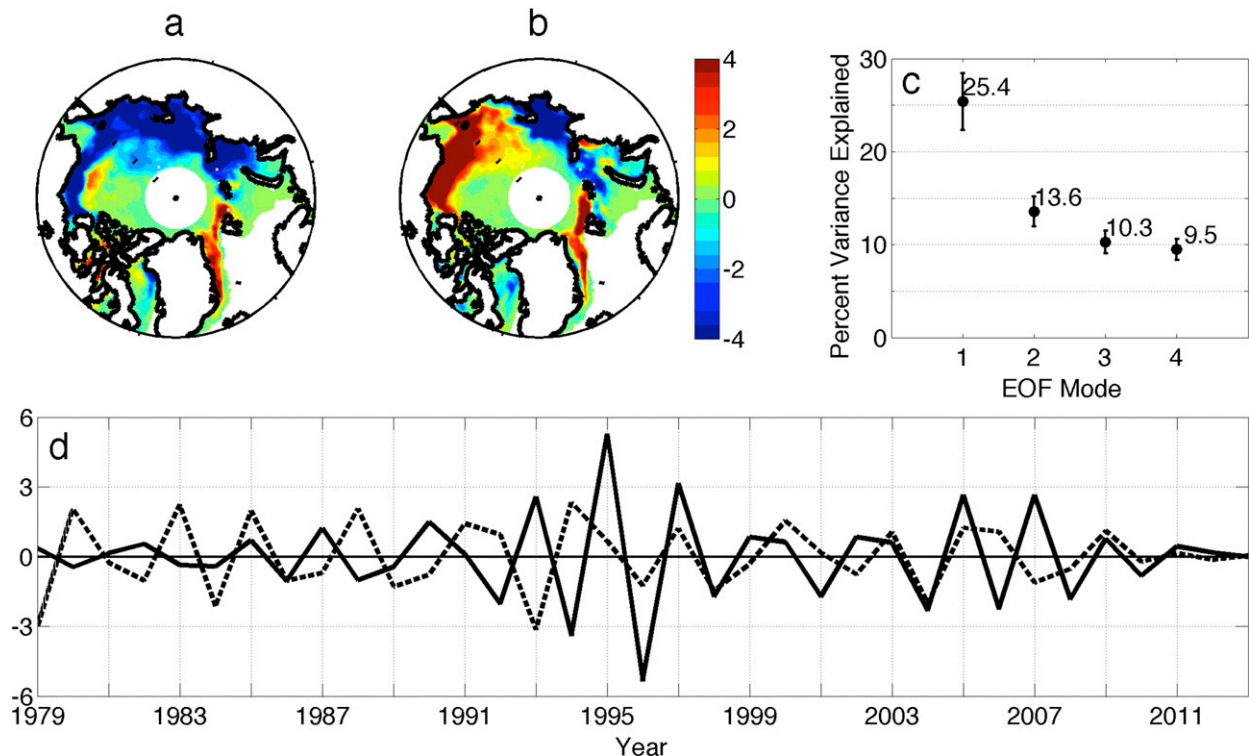


FIG. 3. As in Fig. 2, but for ASO.

monsoon indices were developed to capture rainfall variability throughout the boreal summer and represent the seasonal mean strength of the monsoon. The interannual variability of the EASM is captured by generating an index that represents the dipole behavior of precipitation between the western North Pacific summer monsoon (WNPSM) and EASM. After removing the 3-yr running mean to eliminate low-frequency variability with periods greater than 5 years, the precipitation during the peak months of June and July was standardized and the EASM box (20° – 45° N, 95° – 127.5° E) is subtracted from the WNPSM box (5° – 15° N, 115° – 140° E). A dipole precipitation index is considered since it is a proxy for the anomalous strength of the western North Pacific subtropical high pressure circulation and also captures anomalous heating that generates the teleconnection pattern. Interannual variability during the peak of the ISM is defined using July and August precipitation averaged over 10° – 30° N, 70° – 105° E. To develop difference composites, high and low monsoon rainfall years were determined by finding events in which each index exceeded one-half standard deviation (Table 1). The positive years and negative years were composited and the difference between each was taken.

Using bimonthly averages of rainfall for each index, correlations were performed with the June–August (JJA)

SIC second empirical orthogonal function (EOF2) mode and August–October (ASO) EOF2 time series. These correlations were performed while varying the rainfall periods between April and October. The EASM index correlation was maximized ($r = 0.83$) using June–July precipitation and the June–August SIC EOF2 time series. The ISM index correlation was maximized ($r = 0.77$) using July–August precipitation and the August–October SIC EOF2 time series. These results indicate a nearly instantaneous connection between the EASM and June–August SIC EOF2 and a 1-month lag between ISM precipitation and August–October SIC EOF2.

3. The major modes of interannual SIC variations

The interannual variability of Arctic SIC is examined by removing the 3-yr running mean to eliminate decadal variability and the overall nonlinear declining trend. The 3-yr running mean isolates the interannual frequencies (variability with 2–5-yr periods) that are common along the periphery of the Arctic Ocean during early and late summer (Fig. 1). To derive major modes of interannual SIC variability, EOF analysis is conducted for early summer (June–August) and late summer (August–October), respectively, as these

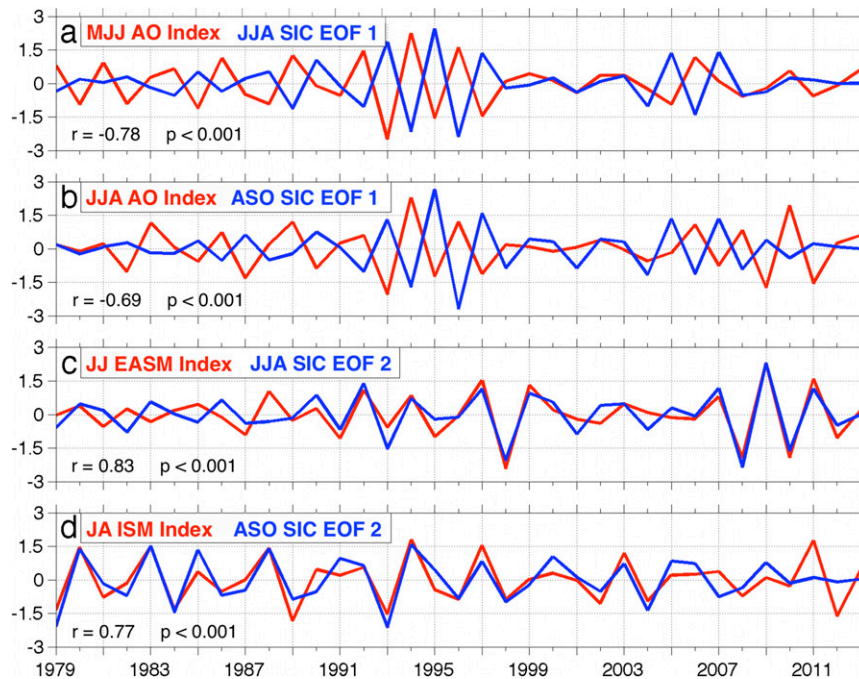


FIG. 4. (a) Time series of standardized May–July (MJJ) AO index plotted against JJA SIC EOF1. (b) Time series of standardized JJA AO index plotted against ASO SIC EOF1. (c) Time series of standardized June–July (JJ) EASM index plotted against JJA SIC EOF2. (d) Time series of standardized July–August (JA) ISM index plotted against ASO SIC EOF2. EASM and ISM indices are defined in section 2. The correlation coefficient and p value are shown in the bottom left.

two periods produced differing EOF2 modes, omit intraseasonal variability, and are statistically distinguishable from the corresponding first and higher modes (North et al. 1982). Originally 2-month aggregates were chosen but they failed to produce early and late summer EOF2 modes that were separable; also, they failed to exhibit a low correlation with one another. The spatial domain for the EOF analysis matches the National Snow and Ice Data Center (NSIDC) polar stereographic projection plane with corners positioned on (30.98°N, 168.35°E), (33.92°N, 279.26°E), (34.35°N, 350.03°E), and (31.37°N, 102.34°E).

The first EOF (EOF1) modes in both periods have similar zonally symmetric patterns along the margins of the Arctic Ocean from the Eurasian Arctic to the Beaufort Sea and exhibit a temporal correlation coefficient of $r = 0.92$ (Figs. 2a and 3a). These EOF1 modes are related to Arctic Oscillation (AO) conditions, which is consistent with previous findings of the local coupling between AO and Arctic sea ice (Singarayer and Bamber 2003; Rigor and Wallace 2004). However, earlier work discovered that the decrease in summer zonally symmetric SIC is linked to the high-phase winter AO (Rigor and Wallace 2004; Rigor et al. 2002), but over the longer period of our analyses we

reveal that the summer SIC EOF1 patterns exhibit a much stronger connection to the AO in the preceding 1–2 months than the earlier winter months. The 3-month averaged AO index during May–July (June–August) and the SIC EOF1 during June–August (August–October) have statistically significant 1–2-month lagged temporal correlations of $r = -0.78$ ($r = -0.69$; Figs. 4a,b). Additionally, a mostly zonal sea ice reduction throughout the Arctic margins is strongly attributed to low AO index values (anomalously high SLP over the Arctic Ocean) as shown by regressions with SLP and sea ice motion vectors (Fig. 5).

The EOF2 modes during the two summer periods have unique zonally asymmetric SIC patterns and are related to Asian monsoon rainfall (Figs. 2b and 3b). The Asian summer monsoon comprises two major components, the ISM and EASM (Wang and Fan 1999). The convective centers and associated heating are located between the Arabian Sea and Bay of Bengal for the ISM and a meridional dipole pattern between subtropical East Asia and tropical South China Sea and Philippine Sea for the EASM (Wang and Fan 1999; Wang et al. 2001). Using spatially averaged precipitation indices to represent the strength of the ISM and EASM, sensitivity calculations were performed to determine the

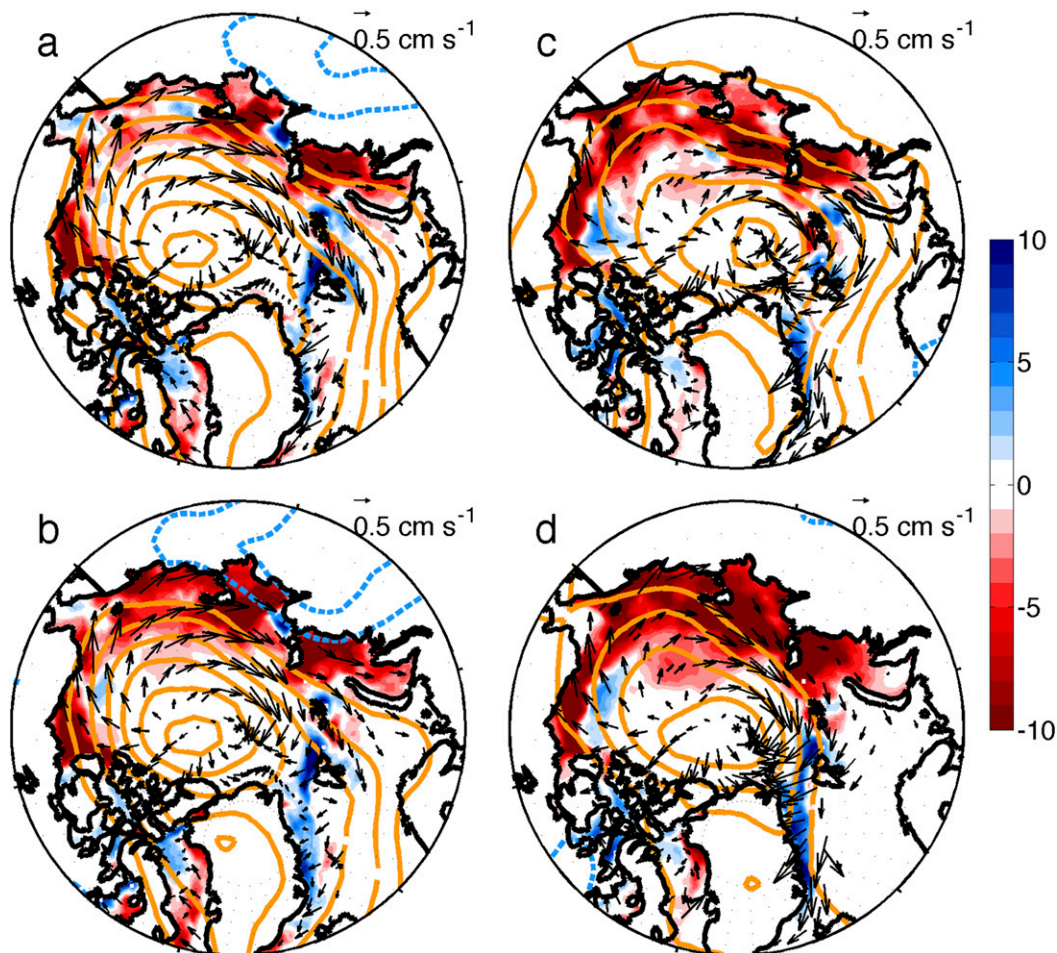


FIG. 5. SIC (shaded) with positive (hPa; orange contours, interval of 0.4 hPa) and negative (hPa; blue contours, interval of 0.4 hPa) SLP anomalies and PIOMAS ice motion vector patterns regressed with the (a) MJJ inverse AO index, (b) JJA EOF1, (c) JJA inverse AO index, and (d) ASO EOF1.

connection between each SIC EOF2 and the corresponding monsoon system. The second EOF mode of SIC in June–August is closely correlated ($r = 0.83$) with peak season (June–July) precipitation in the EASM (Fig. 4c) and the second EOF mode of SIC in August–October exhibits a significant relationship ($r = 0.77$) with the peak season (July–August) precipitation in the ISM (Fig. 4d). The time lag between monsoon precipitation and SIC “response” can be explained by examining the teleconnection patterns of both monsoon systems, which create far-reaching impacts on global climate (Wang et al. 2001; Lau 1992) and the strength of the sea ice forcing mechanisms generated by each monsoon-driven wave train.

4. The EASM–Arctic teleconnection

During years of low EASM rainfall (and simultaneous high rainfall in the western North Pacific), a tripole-like

circulation pattern develops that extends northeastward up the East Asian coast in which an anomalous baroclinic low-level cyclone develops over the Philippine Sea, barotropic anticyclonic circulation anomalies develop over Japan and the Korean Peninsula, and a barotropic cyclonic circulation develops over northeastern Russia (Fig. 6). Over eastern Siberia the wave train bifurcates. The southern branch propagates along a great-circle route across the North Pacific to North America and then along the subtropical jet stream into the North Atlantic, which has been discussed in earlier studies (Nitta 1987; Wang et al. 2000; Lau and Weng 2000a,b; Lau et al. 2004). What was not previously noticed is a northward branch from eastern Siberia into the Arctic Ocean. This northward teleconnection route directly links to the barotropic Arctic high pressure anomalies north of Siberia and Alaska. Using the difference between high and low EASM index years, the low-level geopotential height field

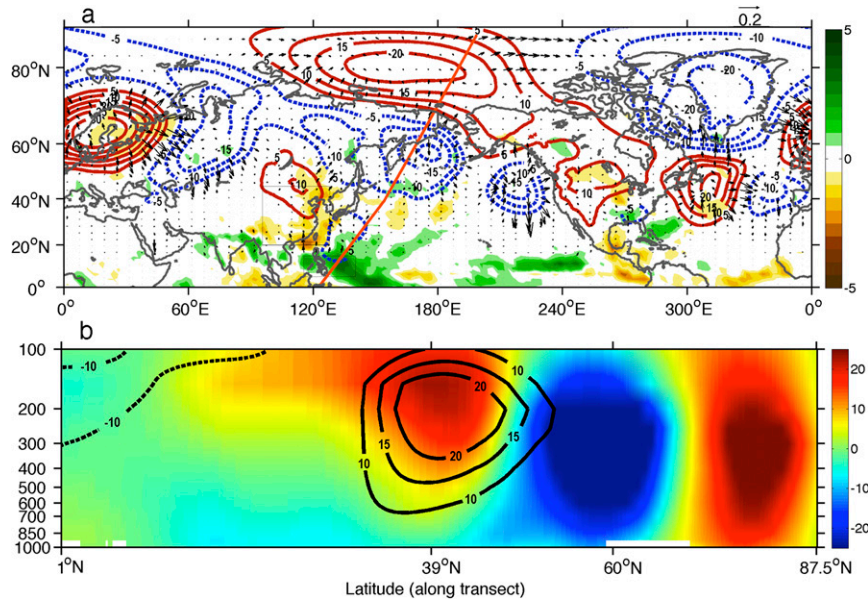


FIG. 6. (a) Positive (m; red contours, interval of 5 m) and negative (m; blue contours, interval of 5 m) 850–700-hPa averaged geopotential height differences between high (8 yr) and low (8 yr) EASM index years and precipitation rate differences (mm day^{-1} ; shaded). Overlaid are wave activity flux vectors ($\text{m}^2 \text{s}^{-2}$) calculated from the composite difference fields. Boxes used to compute each monsoon index are also shown (see section 2). (b) Cross section moving north through the EASM teleconnection pattern [orange line in (a)] showing geopotential height differences (m; shaded) and average zonal component of the wind (m s^{-1}).

exhibits a prominent northward energy propagation pathway from Siberia to the Arctic Ocean, as shown by the divergence of the wave activity flux vectors and the transect through the teleconnection pattern (Fig. 6b). Thus, the EASM–Arctic teleconnection consists of four statistically significant (Fig. 7a) anomalous circulation cells: the baroclinic low-level cyclone over the Philippine Sea, barotropic anticyclonic anomalies over Japan and the Korean Peninsula, the barotropic cyclone over eastern Siberia, and the barotropic Arctic anticyclone. The northward-propagating EASM–Arctic teleconnection pattern partially explains the short time lag (less than a month) between anomalous East Asian monsoon heating and teleconnection response.

5. The ISM–Arctic teleconnection

During years of high ISM rainfall, the 300–200-hPa geopotential height field exhibits a different wave energy propagation pattern (Fig. 8). This wave train is largely shared with the circumglobal teleconnection (CGT) response to the ISM heating that displays a wavenumber-6 pattern with variability centers closely matching those discussed in an earlier study (Ding and Wang 2005). The proximity of ISM heating relative to the subtropical jet creates a strong coupling that produces a statistically significant downstream wave

train, with the jet stream acting as a waveguide due to the strong vorticity gradients along jet margins (Hsu and Lin 1992; Hoskins and Ambrizzi 1993; Figs. 7b and 8). The subtropical jet stream allows upstream extratropical wave activity to enter the jet exit region over the North Atlantic, where the zonally varying flow produces strong barotropic instability, which further amplifies the wave train (Simmons et al. 1983). This is verified using transects along the teleconnection route, which show an enhancement of the barotropic circulation over the North Pacific Ocean and a much greater enhancement over the North Atlantic. Note that over the North Atlantic and northwestern Europe, the wave energy bifurcates out of a strong anticyclonic feature. The southeastward propagation route into southern Eurasia and northern Pakistan has been noted previously (Ding and Wang 2005) and is a key component completing the ISM CGT. Of greater interest is a northeastward-propagating branch of wave energy from the North Atlantic into the Arctic (Iwao and Takahashi 2008; Zhu et al. 2011) following the weaker subpolar jet (Orsolini et al. 2015; Fig. 9) to link the anomalous ISM teleconnection with Arctic variability. The Rossby wave train produces a barotropic cyclone covering the Norwegian Sea to northeastern Asia and a barotropic anticyclone extending from Siberia into northern Canada (Fig. 8). Unlike the EASM–Arctic teleconnection pattern, which

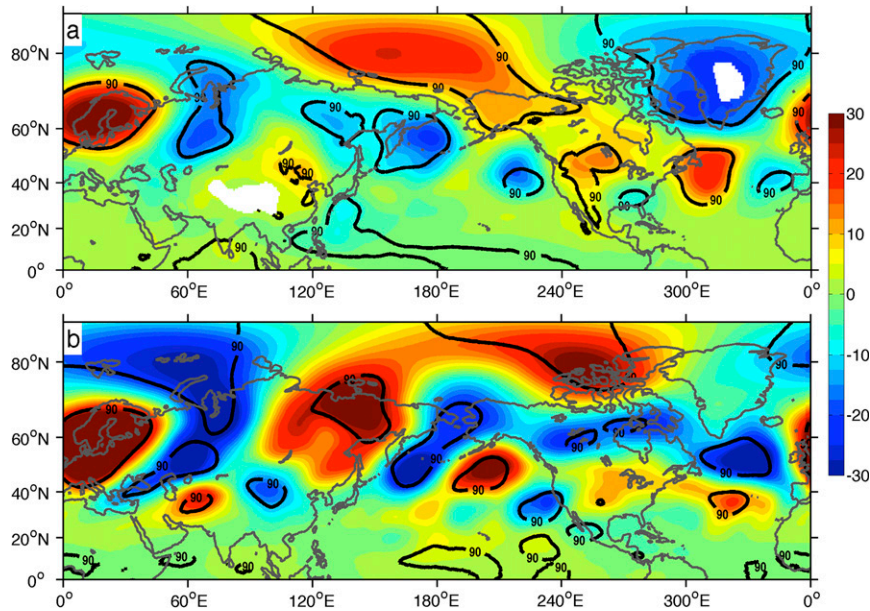


FIG. 7. Geopotential height differences (m) between high and low index years for the (a) EASM using heights averaged between 850 and 700 hPa and (b) ISM using heights averaged between 300 and 200 hPa. Black line represents 90% significance using the Student's t test. White regions are data voids due to topography within the layer.

directly extends up the East Asian coast, the ISM–Arctic teleconnection must travel a significant portion of the Northern Hemisphere zonally along the subtropical jet before extending northward from the North Atlantic Ocean jet exit region and generating polar features. This could partially explain the 1-month lag between July–August ISM rainfall and the related Arctic SIC EOF2 pattern in August–October.

6. Arctic response to the Asian monsoon

The anomalous barotropic circulations that are generated by the Asian monsoon in the Arctic are responsible for producing anomalous SIC patterns along the periphery of the Arctic Ocean. The connection between Arctic circulation modulated by each monsoon and SIC patterns is examined by taking the difference between high and low monsoon index years (Table 1) using composites of SLP, 850-hPa winds, sea ice concentration, and ice motion vectors (Fig. 10). The EASM high and low index differences in SLP exhibit anomalous high pressure over the central Arctic Ocean and low pressure over northern Canada and from the European Arctic to North Atlantic Ocean (Fig. 10a). This SLP anomaly pattern, particularly the anomalous high pressure, is part of the EASM–Arctic linkage as shown by its collocation with the northernmost barotropic anticyclone of the four-celled teleconnection (Fig. 6a). The

anomalous sea ice motion vectors closely coincide with the low-level geostrophic flow and partially explain the creation of the SIC patterns.

The ISM-related SIC patterns are observed using the difference in high and low years from the July–August ISM index. In the SLP field, a dipole-like pattern develops over the Arctic with high pressure anomalies from the Siberian Arctic to western North American Arctic and anomalous low pressure north of the European Arctic (Fig. 10b). The arrangement of these SLP features corresponds to the northeastward teleconnection branch after the ISM CGT bifurcation over the North Atlantic Ocean and Europe (Fig. 8a). Positive SLP anomalies over Scandinavia correspond with the barotropic anticyclone where the teleconnection splits (Fig. 8a). Moving northward along the ISM–Arctic linkage, the barotropic cyclone over the Eurasian Arctic is collocated with the low SLP anomalies, while the barotropic anticyclone extending from Siberia to northern Canada corresponds with anomalous high SLP. The configuration of these SLP features drives an anomalous circulation pattern out of the Laptev Sea that separates into two branches of flows, one into the western North American Arctic and the other toward the Fram Strait. Anomalous ice motion vectors closely resemble the geostrophic flow associated with the ISM-related circulation features and explain the SIC patterns.

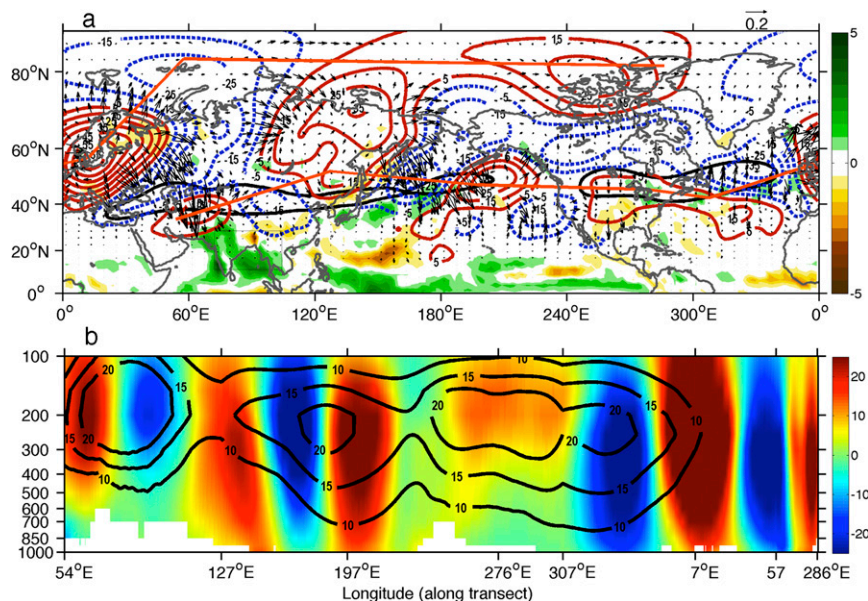


FIG. 8. As in Fig. 6, but for (a) positive (m; red contours, interval of 10 m) and negative (m; blue contours, interval of 10 m) 300–200-hPa averaged geopotential height differences between high (8 yr) and low (11 yr) ISM index years. The black contour outlines the zonal component of the 300–200-hPa averaged wind field (m s^{-1}) demonstrating the climatological JA subtropical jet location. (b) Cross section starting in northwestern India and moving east through the ISM teleconnection pattern [orange line in (a)] showing geopotential height differences (m; shaded) and average zonal component of the wind (m s^{-1}).

Analysis of the PIOMAS reanalysis data reveals the importance of anomalous monsoon-driven advection and thermodynamic processes in shaping the sea ice thickness and concentration patterns. During low EASM rainfall (and high WNPSM rainfall) years, the positive SIC and sea ice thickness (SIT) anomalies in the western North American Arctic are generated through thermodynamic growth and advection of sea ice into this region (Fig. 11). In the Laptev Sea, the divergence of advected sea ice is responsible for reduced sea ice in this region. There is a divergence of ice on the upwind side of the East Siberian Sea while a convergence occurs along the western region of the sea, which is driven by the low-level geostrophic wind along the southern flank of the Arctic barotropic anticyclone and explains the observed anomalous SIC pattern. During high ISM rainfall years, SIC and SIT are reduced from the European Arctic to the Laptev Sea due to advective divergence and thermodynamic melt in this region (Fig. 11). From the Siberian Arctic to the North American Arctic, thermodynamic growth and advection-driven convergence are responsible for increased sea ice in these regions. Strong advective convergence in the Fram Strait and Greenland Sea during high ISM rainfall years is responsible for the anomalous buildup of ice in these regions. The sea ice motion fields and implied geostrophic flow from the anomalous SLP fields demonstrate the apparent relationship between the

monsoon-generated atmospheric conditions and processes that shape the statistically significant SIC patterns (Fig. 12). The advective convergence exhibited by the ISM forcing is smaller in magnitude than the EASM forcing (Fig. 11) due to a weaker surface circulation and ice motion for the ISM (Fig. 10b). The weaker advection exhibited by the ISM could also explain the 1-month lag between the peak of the ISM rainfall and associated interannual sea ice EOF mode since it takes the sea ice anomalies longer to develop in response to the atmospheric forcing.

7. The importance of the remote monsoon forcing

It is essential to realize that although the Asian monsoon-driven SIC variations are the second EOF modes, their importance should not be discounted for the following reasons. First, the leading sea ice EOF modes account for a major portion of the zonally symmetric variation forced locally by the AO, but the second EOF modes account for the largest portion of zonally asymmetric variation of Arctic SIC and the largest SIC response to boreal summer remote forcing. The remotely forced asymmetric pattern could be adding to the complexity of summer sea ice prediction, so understanding it could lead to improved sea ice forecasts. Second, the combined effects of both monsoon

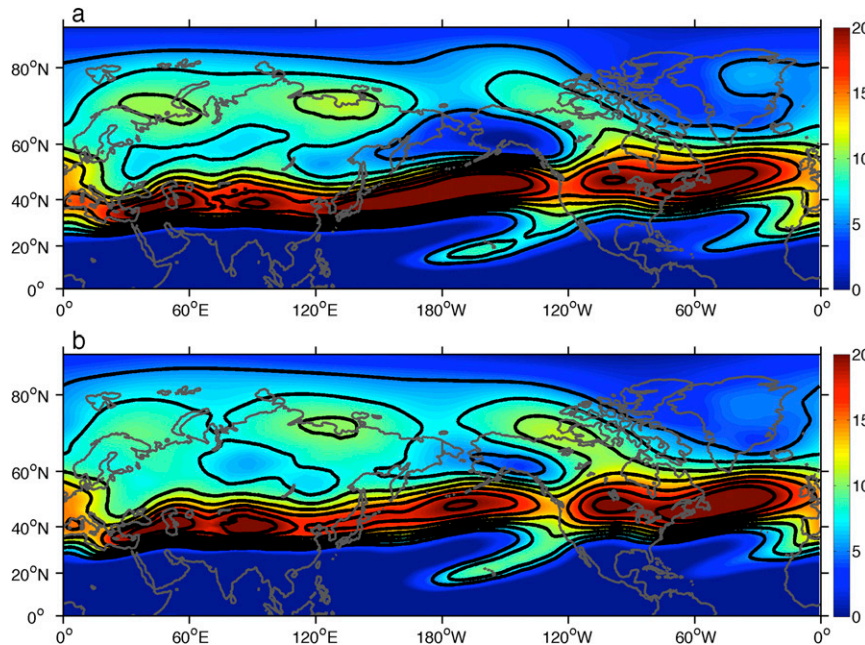


FIG. 9. Climatological zonal component of the 300-hPa wind from ERA-Interim (m s^{-2} ; shaded and contoured with an interval of 2.5 m s^{-2} starting at 5 m s^{-2}) in (a) JJ and (b) JA.

systems over the course of the summer could have large accumulative impacts on the SIC patterns by the end of the melt season, comparable in magnitude to a strong, locally forced AO pattern. To validate this claim, one should note that the two monsoon indices exhibit a positive temporal correlation of $r = 0.52$, significant above the 99% confidence level (Fig. 13). It is more common for the time series of each monsoon index to show identical sign for a given summer, occurring 28 times in the 1979–2013

period, further highlighting the coinciding relationship between both monsoon systems. The SIC monsoon composite differences indicate that congruent phasing of indices would result in numerous occurrences of ISM-forced sea ice patterns enhancing many of the SIC anomalies created by EASM forcing. In the western North American Arctic, the anomalous enhanced sea ice produced during a positive EASM phase can be strengthened by a subsequent positive ISM phase.

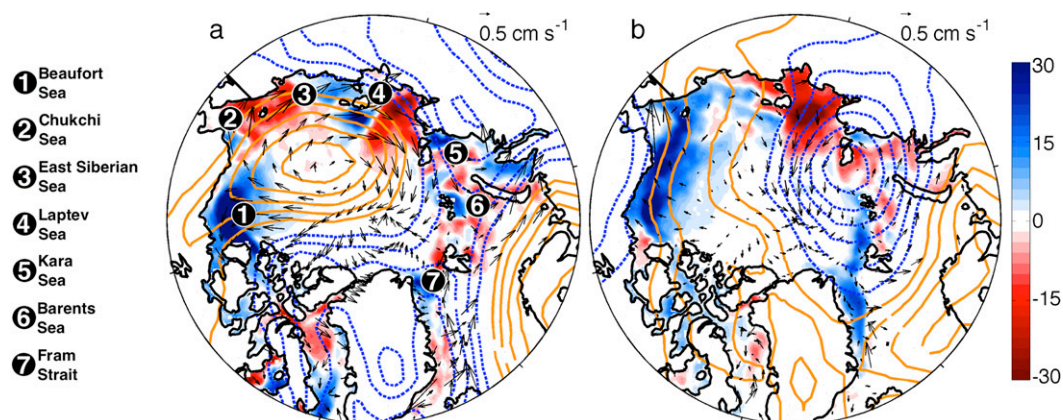


FIG. 10. (a) Differences in high and low EASM index years for JJA SIC (shaded) and positive (hPa; orange contours, interval of 0.4 hPa) and negative (hPa; blue contours, interval of 0.4 hPa) JJ SLP anomalies with JJ PIOMAS ice motion vector patterns. (b) Differences in high and low ISM index years for ASO SIC (shaded) and positive (hPa; orange contours, interval of 0.4 hPa) and negative (hPa; blue contours, interval of 0.4 hPa) JA SLP anomalies with JA PIOMAS ice motion vector patterns. Numbered labels show the locations of regions frequently discussed in the text.

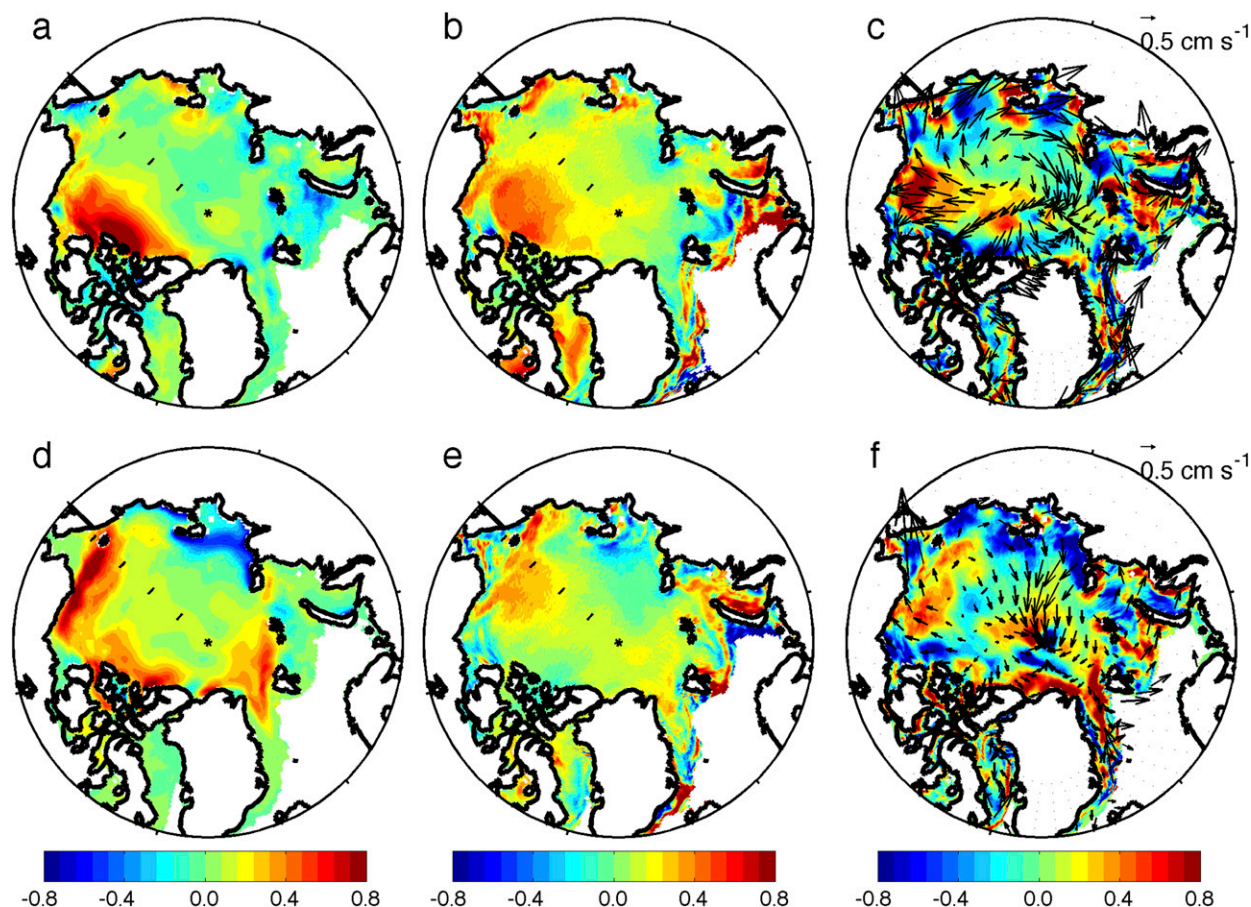


FIG. 11. (left) SIT (m), (center) growth/melt rate due to thermodynamic processes (cm day^{-1}), and (right) growth/decline rate due to advective convergence (cm day^{-1}) and sea ice motion, showing differences between high and low (a)–(c) EASM and (d)–(f) ISM index years.

Additionally, the reduced sea ice anomalies produced in the European Arctic during a positive EASM phase can also be intensified by the following positive ISM forcing. Therefore the accumulative effects of the two monsoon forcings could have a large impact on SIC at the end of the summer melt season.

To further demonstrate this point, SIC composites were created targeting the strongest positive and negative AO years when AO index is greater than one standard deviation from the mean (Figs. 14a,b). Additionally, consecutively strong monsoons (both monsoon indices greater than one-half standard deviation from the mean and must have the same sign) were used to produce SIC composites (Figs. 14c,d). The anomalous September SIC patterns following a strong AO forcing exhibit a mostly zonally uniform pattern extending around the periphery of the Arctic Ocean. Strong monsoon years with identical sign, as identified with our indices, produce a response in which anomalous September sea ice from the Siberian Arctic extending into the North American Arctic contrasts with the response

exhibited over the European Arctic and North Atlantic Ocean. These results indicate that although the remotely forced SIC patterns appear as the second EOF modes, the response following consecutively strong monsoon forcings is comparable to the magnitude and widespread extent of strong locally forced AO patterns. Since the seasonal variation of the two major ASM heat sources is becoming largely predictable, consideration of the combined effects of both monsoons could play a critical role in improving the year-to-year minimum sea ice extent forecasts and understanding the behavior along the ice sheet margins in different regions.

8. Discussion and conclusions

a. Discussion

Summer SIC patterns along the periphery of the Arctic Ocean are driven by remote anomalous thermodynamic and dynamic forcing, which changes as the anomalous EASM and ISM rainfall-driven heating

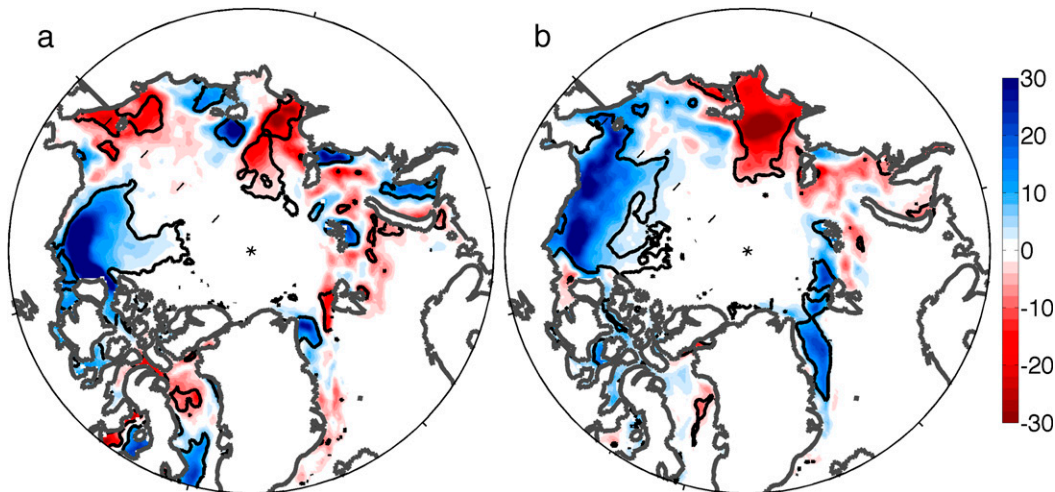


FIG. 12. Differences in high and low (a) EASM and (b) ISM index years for SIC (shaded), and the 99% significance level (contours) using the Student's t test.

progresses and the associated teleconnection patterns modify the polar circulation. Previous work shows that Asian monsoon–forced wave trains travel into surrounding basins through great-circle routes, guided by the polar critical latitude. Observations show that the wave energy associated with the monsoon teleconnections bifurcates, with some wave energy generating an Arctic response while the remainder continues southeastward along the great-circle route. The EASM wave energy bifurcation occurs over northeastern Siberia directly relating anomalous EASM heating with Arctic circulation while the ISM bifurcation develops over the North Atlantic and Europe connecting the circumglobal ISM teleconnection with Arctic variability.

Dynamical modeling of Asian monsoon rainfall has exhibited a low skill ($TCC = 0.35$) in the past 32 years even while using 1 June to initialize (Wang et al. 2015a), and more recently the skill has declined further (Wang et al. 2015b). A new approach using predictable mode analysis (PMA), which decomposes monsoonal rainfall into EOF modes and finds meaningful, physically established predictors, has shown better progress by now representing large-scale climate influences on local precipitation (Wang et al. 2015a). The prediction of EASM rainfall needs further improvement but knowledge of different remote influences on local rainfall in this region is growing (Gong et al. 2011; Wang et al. 2000).

The mechanisms by which anomalous EASM and ISM affect the year-to-year fluctuation of sea ice patterns and polar ice growth and decay may be instrumental for understanding tropical influence on Arctic sea ice in general. Additionally, the remote monsoon–Arctic forcing mechanism could function on

intraseasonal and decadal time scales, and may exert impacts under global climate change. Toward the end of the twenty-first century, the domain, amount, and duration of Asian monsoon precipitation are expected to increase with a warming climate (Lee and Wang 2014), and it is anticipated that this increasing trend could contribute to remotely forced long-term changes in Arctic sea ice patterns. Although the summer Arctic ice extent is expected to continually decline, the monsoon impact will remain an important variability source along the marginal ice sheet zone and will possibly produce lasting impacts into other seasons even after the summer ice completely melts. These hypotheses demonstrate the necessity for future numerical modeling studies once the observed monsoon–Arctic linkages are better replicated.

Year-to-year prediction of summer sea ice concentration and thickness patterns will be a welcome asset given the rapidly growing interest in Arctic resources. The anticipated growth and decline of sea ice in large areas along the Arctic Ocean margins will be a decisive tool for forthcoming Arctic navigation routes, oil and mineral exploration, and local coastal communities concerned with adaptation. Recently, the interseasonal link between Arctic ice coverage and midlatitude weather in the succeeding months is becoming better understood and highlights the significance of the widespread Arctic sea ice feedbacks on the Northern Hemisphere. Our results could lead to a better understanding of the complexities of the global climate system when incorporating the role of summer sea ice.

Using the leading two EOF modes, sensitivity tests similar to those shown in Grunseich and Wang (2016)

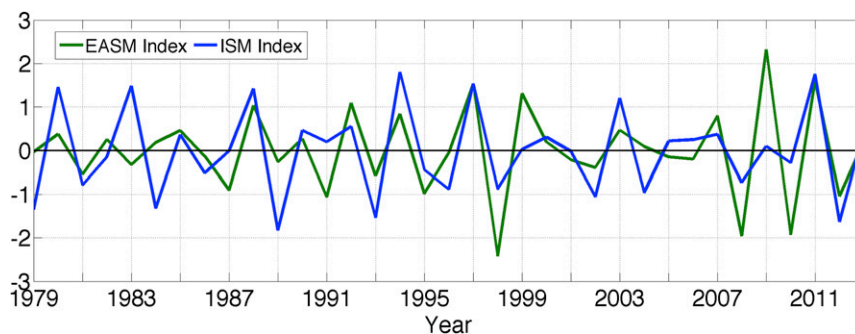


FIG. 13. The JJ EASM index (green) and JA ISM index (blue) are shown for the 1979–2013 period.

are conducted to examine the total possible predictability of interannual sea ice variability during early and late summer and determine the effectiveness of the selected predictors. Each year a prediction is made by multiplying

the standardized predictor or EOF time series with the associated spatial pattern, which acts to scale the respective patterns based on the climate phenomena. The scaled spatial patterns for each mode are combined to

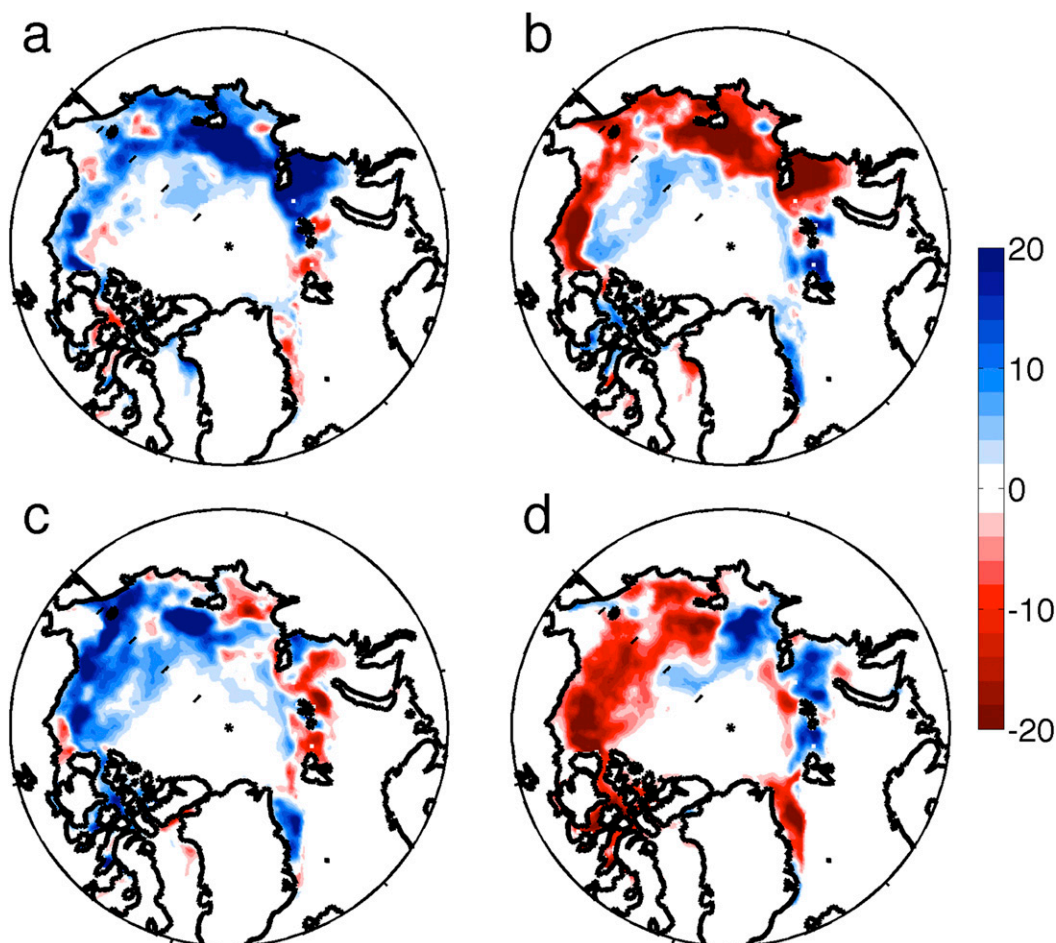


FIG. 14. Composites of SIC anomalies at the end of the September melt season following the strongest (a) positive (7 yr) and (b) negative (6 yr) AO phases. Also shown are composites of anomalous September SIC following consecutively strong (c) positive (5 yr) and (d) negative (5 yr) EASM and ISM monsoons as defined by our indices.

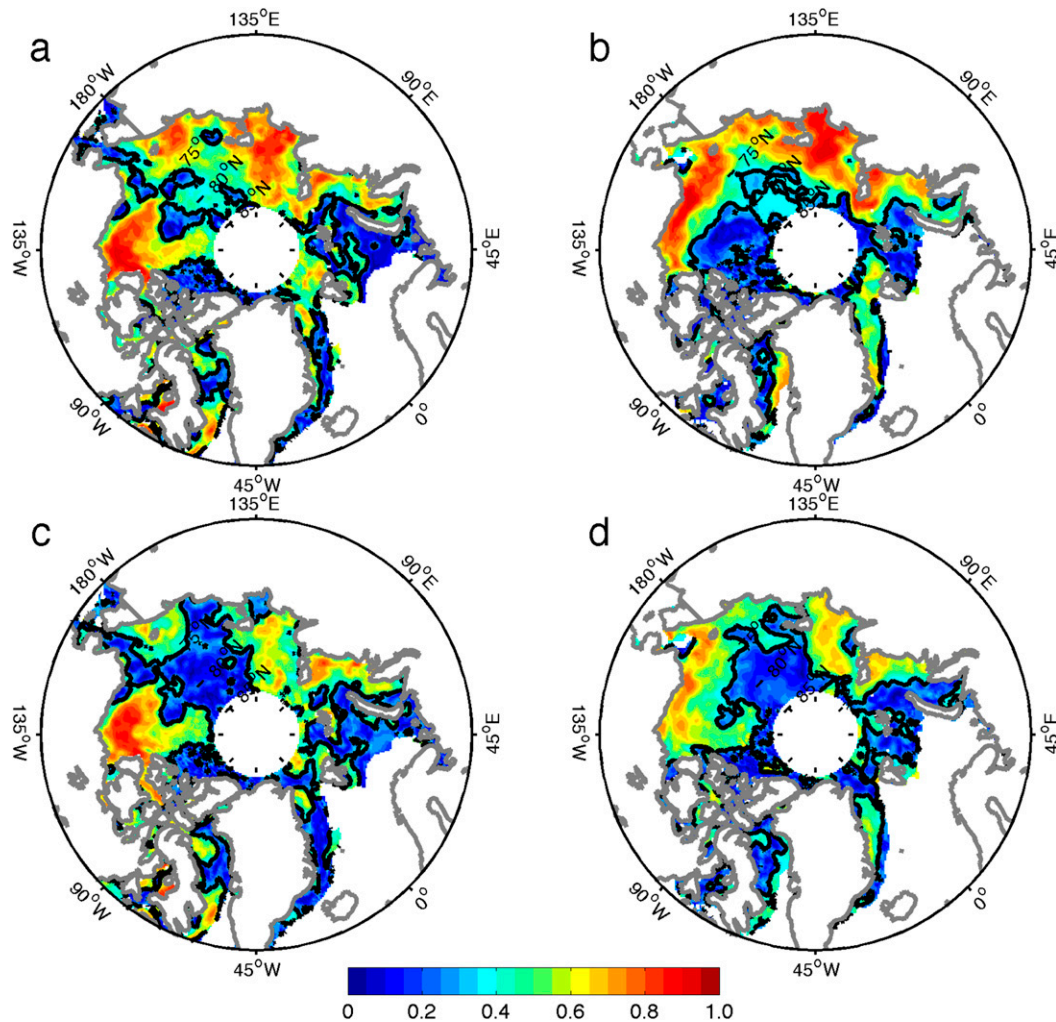


FIG. 15. Correlation coefficients of the combined leading two interannual SIC EOF modes in (a) JJA and (b) ASO with the observed interannual SIC from 1979 to 2013. (c) Correlation coefficients of predicted SIC using the MJJ AO index and JJ EASM predictors with the observed interannual SIC from 1979–2013 in JJA. (d) Correlation coefficients of predicted SIC using the JJA AO index and JA ISM predictors with the observed interannual SIC from 1979–2013 in ASO. Solid contour represents the 95% significance level.

create that summer's prediction for the anomalous sea ice patterns during June–August or August–October. The two leading EOF modes in early (Fig. 15a) and late (Fig. 15b) summer exhibit considerably high correlations throughout the periphery of the inner Arctic Ocean with widespread regions showing $r > 0.8$. The skills of the predictors are assessed using the May–July AO index and June–July EASM index for early summer sea ice and June–August AO index and July–August ISM index for late summer. In early summer (Fig. 15c), the two predictors show high skill in the Beaufort Sea region with correlations exceeding $r > 0.8$. Elsewhere, widespread regions of statistically significant correlations are shown in the eastern East Siberian Sea, Laptev Sea, and Barents Sea. Late summer (Fig. 15d) shows statistically significant

correlations throughout the Arctic margins with the addition of the Greenland Sea region.

The seasonal prediction of Arctic sea ice will draw interdisciplinary scientific interest. The predicted seasonal ice melt pattern could assist biological and environmental scientists in understanding changes in the habitat, migratory patterns, and food resources of local wildlife and marine animals. The seasonal changes in ocean circulation due to the modification of Arctic sea ice patterns will draw the attention of numerous oceanographic disciplines interested in the fluctuations of physical, biogeochemical, and ecological processes. Successful seasonal prediction of Arctic sea ice will be an essential resource that broadens the geosciences and life sciences and provides numerous societal benefits.

b. Conclusions

The interannual variability of summer Arctic sea ice concentration is strongly related to natural forms of local and remote climate variability. The Arctic Oscillation controls the dominant mode of interannual sea ice concentration variability throughout the summer, explaining over 20% of the interannual variance depending upon the time period of the summer season. AO sea ice patterns during the summer months exhibit a mostly zonal uniform pattern of variability following the Arctic margins, which contrasts the Fram Strait and Greenland Sea regions. The summer AO SIC anomalies are shaped through the wind-driven advection of the anomalous monopole circulation center that develops over the Arctic.

The second modes of interannual SIC variability in early and late summer are driven by the East Asian and Indian summer monsoons, respectively. The EASM SIC variability in June–August accounts for 14.3% of the interannual SIC variance and is associated with a dipole pattern along the Arctic margins in which the anomalous sea ice of the eastern East Siberian and Laptev Seas contrasts with the Beaufort Sea anomalies. The ISM sea ice patterns explain 13.6% of the interannual variance and present as a tripole pattern with sea ice in the Laptev Sea contrasting with the Beaufort and Chukchi Seas as well with Fram Strait. The monsoon-driven sea ice patterns are largely shaped through wind-driven advective convergence and appear as SIT and SIC anomalies only after the initiation of each monsoon. The EASM drives the Arctic circulation through a northward-extending meridional teleconnection in which a barotropic circulation is centered over the Arctic. The ISM creates an eastward-propagating circumglobal teleconnection, which is strongly coupled with the subtropical jet, traveling into the North Atlantic where the wave train bifurcates. The northward branch of this bifurcation creates a barotropic dipole circulation pattern over the Arctic and uniquely drives the anomalous sea ice field. During the annual minimum sea ice extent, the combined impacts of strong EASM and ISM forcings can produce sea ice patterns comparable in magnitude and extent to AO-related sea ice anomalies.

Acknowledgments. We acknowledge support from NSF Award AGS-1540783 and NOAA Award NA13OAR4310167. This work is also supported by the Atmosphere–Ocean Research Center supported by Nanjing University of Information Science and Technology and the Global Research Laboratory (GRL) program from the National Research Foundation of Korea Grant 2011-0021927. We acknowledge the

NSIDC, ECMWF, NCEP, and the Polar Science Center for freely providing data. We thank G. Chen for assistance with the wave activity flux calculations. We also thank the three anonymous reviewers for improving the manuscript with constructive comments and feedback.

REFERENCES

- Adler, R. F., and Coauthors, 2003: The Version-2 Global Precipitation Climatology Project (GPCP) monthly precipitation analysis (1979–present). *J. Hydrometeorol.*, **4**, 1147–1167, doi:[10.1175/1525-7541\(2003\)004<1147:TVGPCP>2.0.CO;2](https://doi.org/10.1175/1525-7541(2003)004<1147:TVGPCP>2.0.CO;2).
- Chen, Z., R. Wu, and W. Chen, 2014: Impacts of autumn Arctic sea ice concentration changes on the East Asian winter monsoon variability. *J. Climate*, **27**, 5433–5450, doi:[10.1175/JCLI-D-13-00731.1](https://doi.org/10.1175/JCLI-D-13-00731.1).
- Comiso, J. C., 2000: updated 2015: Bootstrap Sea Ice Concentrations from *Nimbus-7* SMMR and DMSP SSM/I-SSMIS, version 2. NASA DAAC at the National Snow and Ice Data Center. [Available online at http://nsidc.org/data/docs/daac/nsidc0079_bootstrap_seaice.gd.html.]
- Ding, Q., and B. Wang, 2005: Circumglobal teleconnection in the Northern Hemisphere summer. *J. Climate*, **18**, 3483–3505, doi:[10.1175/JCLI3473.1](https://doi.org/10.1175/JCLI3473.1).
- , J. M. Wallace, D. S. Battisti, E. J. Steig, A. J. Gallant, H. J. Kim, and L. Geng, 2014: Tropical forcing of the recent rapid Arctic warming in northeastern Canada and Greenland. *Nature*, **509**, 209–212, doi:[10.1038/nature13260](https://doi.org/10.1038/nature13260).
- Francis, J. A., and S. J. Vavrus, 2012: Evidence linking Arctic amplification to extreme weather in mid-latitudes. *Geophys. Res. Lett.*, **39**, L06801, doi:[10.1029/2012GL051000](https://doi.org/10.1029/2012GL051000).
- Gong, D.-Y., J. Yang, S. J. Kim, Y. Gao, D. Guo, T. Zhou, and M. Hu, 2011: Spring Arctic Oscillation–East Asian summer monsoon connection through circulation changes over the western North Pacific. *Climate Dyn.*, **37**, 2199–2216, doi:[10.1007/s00382-011-1041-1](https://doi.org/10.1007/s00382-011-1041-1).
- Grunseich, G., and B. Wang, 2016: Predictability of Arctic annual minimum sea ice patterns. *J. Climate*, **29**, 7065–7088, doi:[10.1175/JCLI-D-16-0102.1](https://doi.org/10.1175/JCLI-D-16-0102.1).
- Guo, D., Y. Q. Gao, I. Bethke, D. Y. Gong, O. M. Johannessen, and H. J. Wang, 2014: Mechanism on how the spring Arctic sea ice impacts the East Asian summer monsoon. *Theor. Appl. Climatol.*, **115**, 107–119, doi:[10.1007/s00704-013-0872-6](https://doi.org/10.1007/s00704-013-0872-6).
- Hall, A., 2004: The role of surface albedo feedback in climate. *J. Climate*, **17**, 1550–1568, doi:[10.1175/1520-0442\(2004\)017<1550:TROSAF>2.0.CO;2](https://doi.org/10.1175/1520-0442(2004)017<1550:TROSAF>2.0.CO;2).
- Holland, M. M., C. M. Bitz, M. Eby, and A. J. Weaver, 2001: The role of ice–ocean interactions in the variability of the North Atlantic thermohaline circulation. *J. Climate*, **14**, 656–675, doi:[10.1175/1520-0442\(2001\)014<0656:TROIOI>2.0.CO;2](https://doi.org/10.1175/1520-0442(2001)014<0656:TROIOI>2.0.CO;2).
- Hoskins, B. J., and T. Ambrizzi, 1993: Rossby wave propagation on a realistic longitudinally varying flow. *J. Atmos. Sci.*, **50**, 1661–1671, doi:[10.1175/1520-0469\(1993\)050<1661:RWPOAR>2.0.CO;2](https://doi.org/10.1175/1520-0469(1993)050<1661:RWPOAR>2.0.CO;2).
- Hsu, H.-H., and S.-H. Lin, 1992: Global teleconnections in the 250-mb streamfunction field during the Northern Hemisphere winter. *Mon. Wea. Rev.*, **120**, 1169–1190, doi:[10.1175/1520-0493\(1992\)120<1169:GTITMS>2.0.CO;2](https://doi.org/10.1175/1520-0493(1992)120<1169:GTITMS>2.0.CO;2).
- IPCC, 2013: *Climate Change 2013: The Physical Science Basis*. Cambridge University Press, 1535 pp.
- Iwao, K., and M. Takahashi, 2008: A precipitation seesaw mode between northeast Asia and Siberia in summer caused by

- Rossby waves over the Eurasian continent. *J. Climate*, **21**, 2401–2419, doi:[10.1175/2007JCLI1949.1](https://doi.org/10.1175/2007JCLI1949.1).
- Kattsov, V., V. Ryabinin, J. Overland, M. Serreze, M. Visbeck, J. Walsh, W. Meier, and X. Zhang, 2010: Arctic sea ice change: A grand challenge of climate science. *J. Glaciol.*, **56**, 1115–1121.
- Kimura, N., and M. Wakatsuchi, 2000: Relationship between sea-ice motion and geostrophic wind in the Northern Hemisphere. *Geophys. Res. Lett.*, **27**, 3735–3738, doi:[10.1029/2000GL011495](https://doi.org/10.1029/2000GL011495).
- Krishnamurti, T. N., R. Krishnamurti, S. Das, V. Kumar, A. Jayakumar, and A. A. Simon, 2015: Pathway connecting the monsoonal heating to the rapid Arctic ice melt. *J. Atmos. Sci.*, **72**, 5–34, doi:[10.1175/JAS-D-14-0004.1](https://doi.org/10.1175/JAS-D-14-0004.1).
- Lau, K. M., 1992: The East Asian summer monsoon rainfall variability and climate teleconnection. *J. Meteor. Soc. Japan*, **70**, 211–241.
- , and H. Weng, 2000a: Remote forcing of US summertime droughts and floods by the Asian monsoon? *GEWEX News*, No. 10, International GEWEX Project Office, Silver Spring, MD, 5–6.
- , and —, 2000b: Teleconnection linking summertime rainfall variability over North America and East Asia. *CLIVAR Exchanges*, No. 5, International CLIVAR Project Office, Southampton, United Kingdom, 18–20.
- , K. M. Kim, and J. Y. Lee, 2004: Interannual variability, global teleconnection and potential predictability associated with the Asian summer monsoon. *East Asian Monsoon*, C. P. Chang, Ed., World Scientific, 153–176.
- Lee, J.-Y., and B. Wang, 2014: Future change of global monsoon in the CMIP5. *Climate Dyn.*, **42**, 101–119, doi:[10.1007/s00382-012-1564-0](https://doi.org/10.1007/s00382-012-1564-0).
- Madden, R. A., and P. R. Julian, 1972: Description of global-scale circulation cells in the tropics with a 40–50 day period. *J. Atmos. Sci.*, **29**, 1109–1123, doi:[10.1175/1520-0469\(1972\)029<1109:DOGSCC>2.0.CO;2](https://doi.org/10.1175/1520-0469(1972)029<1109:DOGSCC>2.0.CO;2).
- Mori, M., M. Watanabe, H. Shiogama, J. Inoue, and M. Kimoto, 2014: Robust Arctic sea-ice influence on the frequent Eurasian cold winters in past decades. *Nat. Geosci.*, **7**, 869–873, doi:[10.1038/ngeo2277](https://doi.org/10.1038/ngeo2277).
- Nitta, T., 1987: Convective activities in the tropical western Pacific and their impact on the Northern Hemisphere summer circulation. *J. Meteor. Soc. Japan*, **65**, 373–390.
- North, G. R., T. L. Bell, R. F. Cahalan, and F. J. Moeng, 1982: Sampling errors in the estimation of empirical orthogonal functions. *Mon. Wea. Rev.*, **110**, 699–706, doi:[10.1175/1520-0493\(1982\)110<0699:SEITEO>2.0.CO;2](https://doi.org/10.1175/1520-0493(1982)110<0699:SEITEO>2.0.CO;2).
- Orsolini, Y. J., L. Zhang, D. H. W. Peters, K. Fraerich, X. Zhu, A. Schneidereit, and B. van den Hurk, 2015: Extreme precipitation events over north China in August 2010 and their link to eastward-propagating wave-trains across Eurasia: Observations and monthly forecasting. *Quart. J. Roy. Meteor. Soc.*, **141**, 3097–3105, doi:[10.1002/qj.2594](https://doi.org/10.1002/qj.2594).
- Plumb, R. A., 1985: On the three-dimensional propagation of stationary waves. *J. Atmos. Sci.*, **42**, 217–229, doi:[10.1175/1520-0469\(1985\)042<0217:OTTDPO>2.0.CO;2](https://doi.org/10.1175/1520-0469(1985)042<0217:OTTDPO>2.0.CO;2).
- Rigor, I. G., and J. M. Wallace, 2004: Variations in the age of Arctic sea-ice and summer sea-ice extent. *Geophys. Res. Lett.*, **31**, L09401, doi:[10.1029/2004GL019492](https://doi.org/10.1029/2004GL019492).
- , —, and R. L. Colony, 2002: Response of sea ice to the Arctic Oscillation. *J. Climate*, **15**, 2648–2663, doi:[10.1175/1520-0442\(2002\)015<2648:ROSITT>2.0.CO;2](https://doi.org/10.1175/1520-0442(2002)015<2648:ROSITT>2.0.CO;2).
- Screen, J. A., 2013: Influence of Arctic sea ice on European summer precipitation. *Environ. Res. Lett.*, **8**, 044015, doi:[10.1088/1748-9326/8/4/044015](https://doi.org/10.1088/1748-9326/8/4/044015).
- , and I. Simmonds, 2010: The central role of diminishing sea ice in recent Arctic temperature amplification. *Nature*, **464**, 1334–1337, doi:[10.1038/nature09051](https://doi.org/10.1038/nature09051).
- Simmons, A., J. Wallace, and G. Branstator, 1983: Barotropic wave propagation and instability, and atmospheric teleconnection patterns. *J. Atmos. Sci.*, **40**, 1363–1392, doi:[10.1175/1520-0469\(1983\)040<1363:BWPAIA>2.0.CO;2](https://doi.org/10.1175/1520-0469(1983)040<1363:BWPAIA>2.0.CO;2).
- Singarayer, J. S., and J. L. Bamber, 2003: EOF analysis of three records of sea-ice concentration spanning the last 30 years. *Geophys. Res. Lett.*, **30**, 1251, doi:[10.1029/2002GL016640](https://doi.org/10.1029/2002GL016640).
- Stroeve, J. C., L. C. Hamilton, C. M. Bitz, and E. Blanchard-Wrigglesworth, 2014: Predicting September sea ice: Ensemble skill of the SEARCH Sea Ice Outlook 2008–2013. *Geophys. Res. Lett.*, **41**, 2411–2418, doi:[10.1002/2014GL059388](https://doi.org/10.1002/2014GL059388).
- Thorndike, A. S., and R. Colony, 1982: Sea ice motion in response to geostrophic winds. *J. Geophys. Res.*, **87**, 5845–5852, doi:[10.1029/JC087iC08p05845](https://doi.org/10.1029/JC087iC08p05845).
- , D. A. Rothrock, G. A. Maykut, and R. Colony, 1975: The thickness distribution of sea ice. *J. Geophys. Res.*, **80**, 4501–4513, doi:[10.1029/JC080i033p04501](https://doi.org/10.1029/JC080i033p04501).
- Wang, B., and Z. Fan, 1999: Choice of South Asian summer monsoon indices. *Bull. Amer. Meteor. Soc.*, **80**, 629–638, doi:[10.1175/1520-0477\(1999\)080<0629:COSASM>2.0.CO;2](https://doi.org/10.1175/1520-0477(1999)080<0629:COSASM>2.0.CO;2).
- , R. Wu, and X. Fu, 2000: Pacific–East Asian teleconnection: How does ENSO affect East Asian climate? *J. Climate*, **13**, 1517–1536, doi:[10.1175/1520-0442\(2000\)013<1517:PEATHD>2.0.CO;2](https://doi.org/10.1175/1520-0442(2000)013<1517:PEATHD>2.0.CO;2).
- , —, and K.-M. Lau, 2001: Interannual variability of the Asian summer monsoon: Contrasts between the Indian and the western North Pacific–East Asian monsoon. *J. Climate*, **14**, 4073–4090, doi:[10.1175/1520-0442\(2001\)014<4073:IVOTAS>2.0.CO;2](https://doi.org/10.1175/1520-0442(2001)014<4073:IVOTAS>2.0.CO;2).
- , J.-Y. Lee, and B. Xiang, 2015a: Asian summer monsoon rainfall predictability: A predictable mode analysis. *Climate Dyn.*, **44**, 61–74, doi:[10.1007/s00382-014-2218-1](https://doi.org/10.1007/s00382-014-2218-1).
- , B. Xiang, J. Li, P. J. Webster, M. N. Rajeevan, J. Liu, and K.-J. Ha, 2015b: Rethinking Indian monsoon rainfall prediction in the context of recent global warming. *Nature Comm.*, **6**, 7154, doi:[10.1038/ncomms8154](https://doi.org/10.1038/ncomms8154).
- Xie, P., and P. A. Arkin, 1997: Global precipitation: A 17-year monthly analysis based on gauge observations, satellite estimates, and numerical model outputs. *Bull. Amer. Meteor. Soc.*, **78**, 2539–2558, doi:[10.1175/1520-0477\(1997\)078<2539:GPAYMA>2.0.CO;2](https://doi.org/10.1175/1520-0477(1997)078<2539:GPAYMA>2.0.CO;2).
- Yim, S. Y., B. Wang, J. Liu, and Z. Wu, 2014: A comparison of regional monsoon variability using monsoon indices. *Climate Dyn.*, **43**, 1423–1437, doi:[10.1007/s00382-013-1956-9](https://doi.org/10.1007/s00382-013-1956-9).
- Yoo, C., S. Feldstein, and S. Lee, 2011: The impact of the Madden–Julian oscillation trend on the Arctic amplification of surface air temperature during the 1979–2008 boreal winter. *Geophys. Res. Lett.*, **38**, L24804, doi:[10.1029/2011GL049881](https://doi.org/10.1029/2011GL049881).
- , S. Lee, and S. B. Feldstein, 2012: Arctic response to an MJO-like tropical heating in an idealized GCM. *J. Atmos. Sci.*, **69**, 2379–2393, doi:[10.1175/JAS-D-11-0261.1](https://doi.org/10.1175/JAS-D-11-0261.1).
- Zhang, J., and D. A. Rothrock, 2003: Modeling global sea ice with a thickness and enthalpy distribution model in generalized curvilinear coordinates. *Mon. Wea. Rev.*, **131**, 845–861, doi:[10.1175/1520-0493\(2003\)131<0845:MGSIIWA>2.0.CO;2](https://doi.org/10.1175/1520-0493(2003)131<0845:MGSIIWA>2.0.CO;2).
- Zhu, X., O. Bothe, and K. Fraedrich, 2011: Summer atmospheric bridging between Europe and East Asia: Influences on drought and wetness on the Tibetan Plateau. *Quat. Int.*, **236**, 151–157, doi:[10.1016/j.quaint.2010.06.015](https://doi.org/10.1016/j.quaint.2010.06.015).